Revealing dynamic-mechanical properties of precipitates in a nanostructured thin film using micromechanical spectroscopy

Markus Alfreider,* Michael Meindlhumer, Tobias Ziegelwanger, Rostislav Daniel, Jozef Keckes, and Daniel Kiener

Nanostructured materials with their remarkable properties are key enablers in many modern applications. For example, industrial dry-milling processes would not be as widely spread without the use of hard, wear-resistant metal nitride coatings to protect the cutting tools. However, improving these nanostructured thin films with regard to dynamical properties is demanding as probing respective parameters of (sub-)micron layers without any substrate influence is still challenging. To extend the scientific toolbox for such spatially confined systems, a novel methodological approach based on resonance peak measurements of a cantilever-transducer system termed micromechanical spectroscopy (µMS) is developed and applied to a $Al_{0.8}Cr_{0.2}N$ model system. The mainly wurtzite type supersaturated $Al_{0.8}Cr_{0.2}N$ system showed precipitation of cubic CrN at grain boundaries and local Cr variations upon annealing at 1050°C. This was accompanied by an increase in the previously unknown damping capability of 63 percent and an increase in Young's modulus by 36 percent.

Impact statement

There is a wide variety of applications for nano- to micrometer-sized thin films in today's engineering technology, from thermal barrier- and wear-resistant coatings in turbines and bearings, over diffusion barriers and heatsinks in microelectronic devices, to optically active layers in lasers or mirrors. The mechanical properties of such thin films are oftentimes governed by their thermal history, leading to either intentional or undesired changes in the microstructure (e.g., the formation of precipitates). While the investigation of such features is usually constricted to static analysis using high-resolution techniques, such as transmission electron microscopy, understanding their impact on dynamic properties of the film remains a challenge. However, these are highly relevant in many engineering applications where cyclic behavior is common, such as high-speed dry milling. In the present work, we investigate the change in mechanical damping capability upon annealing of a 6-µm thin AlCrN film, commonly used in demanding dry-milling applications, using micromechanical spectroscopy (µMS) of cantilever-shaped specimens. After a carefully adjusted heat treatment, the film exhibits the formation of cubic CrN precipitates in an otherwise wurtzite AlCrN matrix, which leads to a previously unknown beneficial increase in damping capability of the film.

Introduction

Hard nanoceramic coatings are commonly used in modern engineering applications where durability and thermal stability matter, such as cutting inserts for high-speed dry milling[1,2] or thermal barrier coatings for turbines.[3–5]

Commonly, such systems are based on transition-metal nitride thin films such as TiN and CrN deposited by plasma-assisted physical vapor deposition techniques (e.g., cathodic arc evaporation).[6] Adding Al into TiN and CrN leads to the formation of $Ti_{1-x}Al_xN$ and $Cr_{1-x}Al_xN$, respectively, which have significantly higher hardness and oxidation resistance compared to their representative binary counterparts.[7] In turn, cubic (B1) $Ti_{1-x}Al_xN$ and $Cr_{1-x}Al_xN$ form metastable supersaturated solid solutions, where Al replaces Ti or Cr up to $x = 0.67$[8,9] or 0.7,[7] respectively. Upon annealing, these thin films undergo a complex temperature and (residual) strain-dependent decomposition processes,[10,11] which alter their functional and mechanical properties.[7] Typically, for $Ti_{1-x}Al_xN$ spinodal decomposition into Ti-rich and Al-rich cubic zones is observed at temperatures between 800° and 900°C leading to a slight increase of hardness[12] and toughness,[13] while after exceeding 950°C, the formation of wurtzite (B4) Al(Ti)N is promoted, resulting in a significant drop in mechanical properties.[12–14] Comparably, cubic $Cr_{1-x}Al_xN$ ($x < 0.7$) directly

Markus Alfreider, Department of Materials Science, Montanuniversität Leoben, Leoben, Austria; markus.alfreider@unileoben.ac.at
Michael Meindlhumer, Department of Materials Science, Montanuniversität Leoben, Leoben, Austria
Tobias Ziegelwanger, Department of Materials Science, Montanuniversität Leoben, Leoben, Austria
Rostislav Daniel, Department of Materials Science, Montanuniversität Leoben, Leoben, Austria
Jozef Keckes, Department of Materials Science, Montanuniversität Leoben, Leoben, Austria
Daniel Kiener, Department of Materials Science, Montanuniversität Leoben, Leoben, Austria
*Corresponding author

decomposes into cubic Cr(Al)N and wurtzite Al(Cr)N at temperatures above ~700–900°C, where the former transforms later on at temperatures surpassing 1000°C and 1350°C into Cr_2N and metallic Cr under the release of gaseous nitrogen.[15]

In the case of $Cr_{1-x}Al_xN$ thin films with $x > 0.7$, the films form predominantly a wurtzite B4 crystal structure during deposition,[9] where Cr replaces Al in the wurtzite crystal structure. There, decomposition starts at significantly higher temperatures (>950°C), forming again cubic Cr(Al)N and wurtzite Al(Cr)N composite.[16,17] As shown for $Al_{0.9}Cr_{0.1}N$, vacuum annealing at 1100°C resulted in the formation of globular cubic Cr(Al)N and elongated cubic CrN precipitates at intra- and intergranular positions, which, in turn, simultaneously enhanced Young's modulus, hardness, fracture stress, and fracture toughness.[17]

The thickness of these films is typically in the range of a few micrometers, which makes the characterization of mechanical properties without substrate influence generally challenging. In recent years, various methods have been developed to obtain reliable experimental data, from hardness and modulus using nanoindentation,[18] over fracture properties using pillar splitting[19] or microcantilever bending[20] to residual stresses using layer removal[21–23] or cross-sectional x-ray nanodiffraction techniques.[24–26] However, all of these approaches determine quasistatic material parameters, whereas in most applications (e.g., high-speed dry milling), these systems are loaded with a rather strong dynamic component due to the high rotation speeds. In fact, dynamic properties such as damping can have a beneficial or detrimental impact on the performance. Higher damping capabilities enable the dissipation of vibrational energy, which could occur through slight eccentricities and misalignments.

Furthermore, damping controls dissipation of energy given reversible elastic deformation and is therefore nondestructive independent of measurement technique. This means that damping measurements can be used to determine inherent changes due to thermal or environmental history in a system, and because a change in damping capability is commonly the direct result of microstructural changes it can be used to probe microstructural modifications, such as precipitation or grain growth.

Although such investigations can be experimentally realized on whole devices (e.g., cutting inserts), the results are challenging to resolve into the individual constituents of the system (e.g., substrate or hard nanoceramic coating). Therefore, it would be desirable to have a technique capable of resolving the damping behavior of these individual constituents.

In this article, we showcase such an experimental approach, termed micromechanical spectroscopy (μMS, recently introduced in Reference 27), on a $Al_{0.8}Cr_{0.2}N$ coating on cemented carbide as commonly found in the high-speed dry-milling industry. The measurements are based on determining resonance peaks of an *in situ* nanoindentation transducer system in contact with a cantilever-shaped microspecimen of the coating material inside a scanning electron microscope (SEM). The absence of air-damping inside the SEM chamber enables a high-resolution analysis of the resonance peak and therefore determination of the damping capability of such spatially confined specimens. The measured change in damping upon heat treatment of the coating is correlated to the formation of precipitates using μMS investigations in concert with complementary transmission electron microscopy (TEM) and x-ray diffraction (XRD), respectively.

Results

Microstructural and chemical analysis

Figure 1a shows a cross-sectional SEM image of the $Al_{0.8}Cr_{0.2}N$ film in as-deposited condition. There, individual bright features correspond to residual Cr_xAl_y droplets from the deposition process. Upon annealing for only 5 min at 1050°C, the microstructure exhibits obvious precipitation, as evident by the dark and bright (depending on channeling contrast) features in Figure 1b. Detailed scanning transmission electron microscope (STEM) images in conjunction with energy-dispersive spectroscopy (EDS) analysis, as depicted in Figure 1c reveal a layered microstructure with a slight undulating magnitude of Al and Cr contents, respectively. This layer formation is known to be resultant of the distribution of chemical species inside the deposition plasma in conjunction with the rotation of the substrate in and out of the line of sight of the cathode.[28–30] Furthermore, it is evident that droplets (Figure 1c, bright feature) appear to be mainly intermetallic Cr_xAl_y, as the N content is diminished in that region, while it is approximately constant everywhere else. Thus, with the exception of individual droplets, the film appears to be fully homogenous, suggesting a very high content of supersaturated wurtzite type $Al_{0.8}Cr_{0.2}N$, as detailed in previous works.[17] After heat treatment the film exhibits a clear decomposition, displayed in Figure 1d, where distinct Cr-rich precipitates are evident. These appear to nucleate preferentially at the positions of previously higher initial Cr content (i.e., along the Cr-enriched layers).

Phase analysis

To analyze the phase contents in as-deposited and heat-treated conditions, XRD investigations were conducted on the respective films and are summarized in **Figure** 2. There the peak positions of wurtzite AlN and cubic CrN are denoted by green deltoids and blue squares, respectively. The positions of the WC substrate (gray triangles) and the TiN bonding layer (orange squares) are additionally added for reference. It is evident that the distinct AlN peaks (100: 33.211°; 101: 37.924°; 110: 59.338°) are shifted toward lower values in the as-deposited state and move toward their equilibrium positions upon annealing, in accordance with previous works on comparable composition.[17] However, a contribution of the removal of residual stress by defect annihilation as a consequence of the heat treatment cannot be excluded from the peak shift of
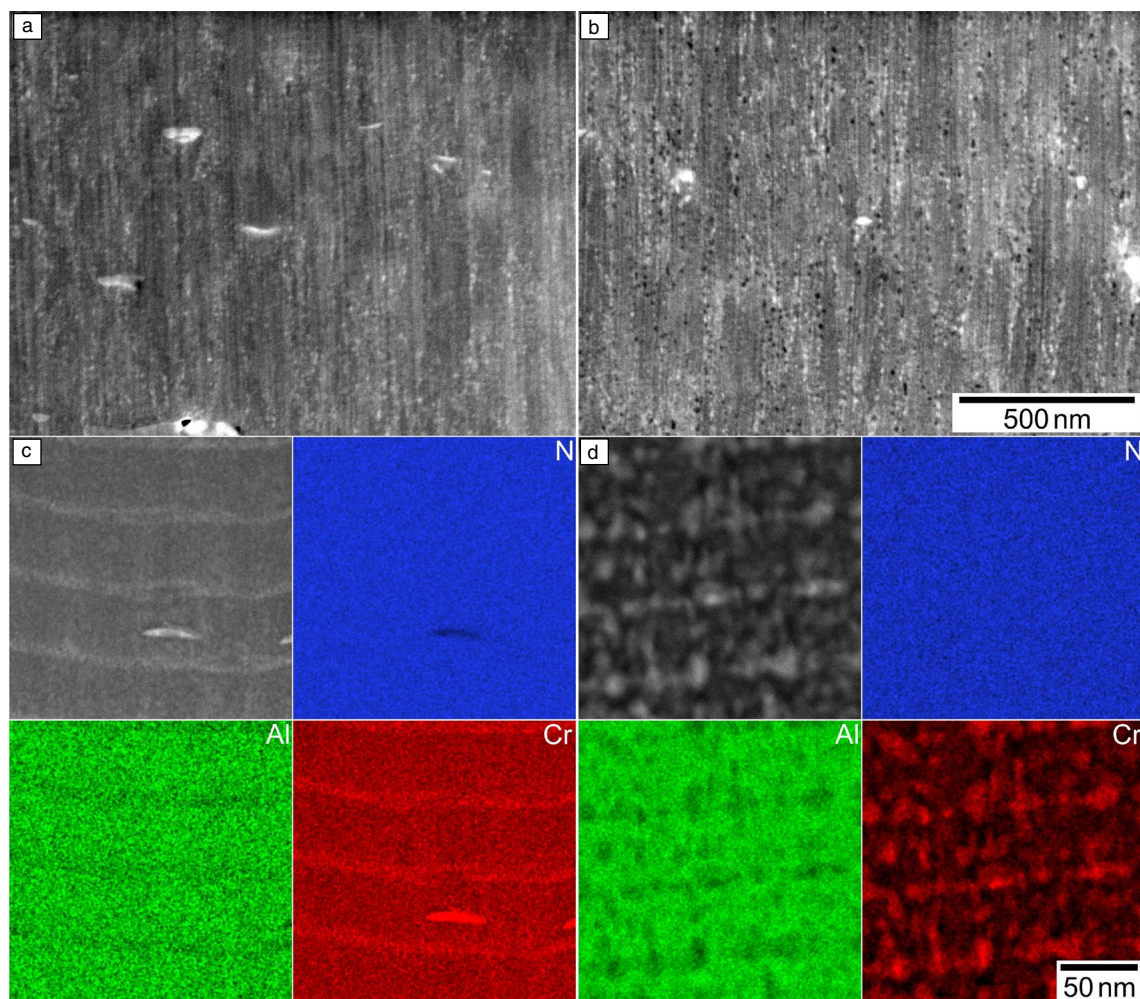
Figure 1. Scanning electron microscope images of (a) the as-deposited and (b) heat-treated $Al_{0.8}Cr_{0.2}N$ films, respectively. The lower part of the figure contains scanning transmission electron microscope micrographs, with corresponding energy-dispersive spectroscopy data of N (blue, top right), Al (green, lower left), and Cr (red, lower right) for (c) as-deposited and (d) heat-treated states, respectively.

the AlN lattice.[17] In fact, the peak shift together with the concomitant increase in magnitude of the 200 CrN peak at 43.693° (**Figure 2**, top right inset) suggests that Cr diffuses out of the supersaturated $Al_{0.8}Cr_{0.2}N$ structure, leaving a relatively higher content of Al in the wurtzite AlN lattice, while the precipitated Cr forms cubic CrN crystals.

Micromechanical spectroscopy
Micromechanical spectroscopic (µMS) investigations were conducted on four as-deposited and three heat-treated cantilever-shaped specimens. This technique was developed recently in a previous work[27] and is capable of revealing changes in damping capability of very confined volumes by investigating the shape of the first resonance peak of the used indentation setup. **Figure 3**a depicts an SEM micrograph of the specimen and indentation setup with relevant geometric dimensions: length L, height W, and thickness B (in imaging direction). Quantitative values
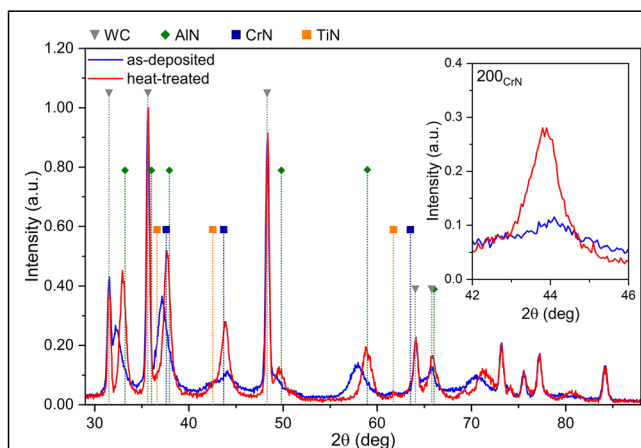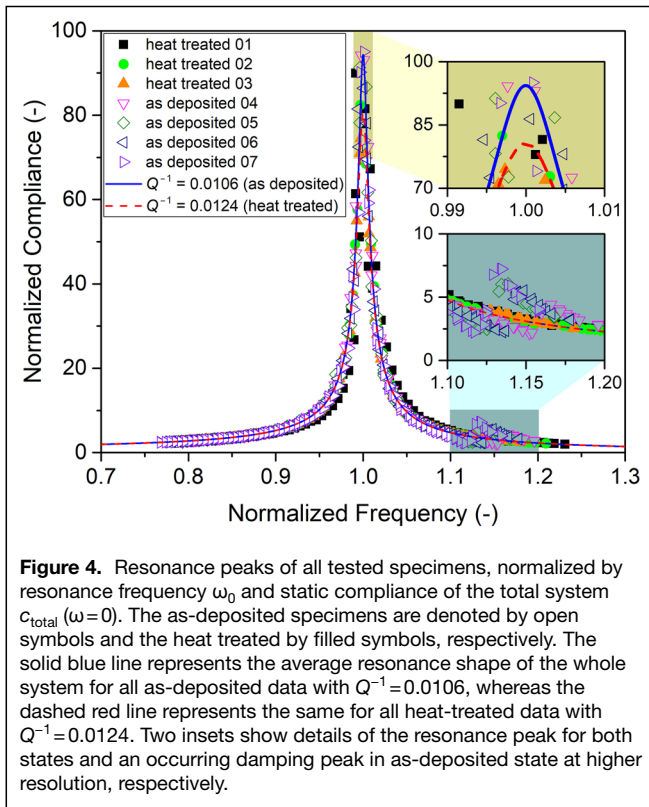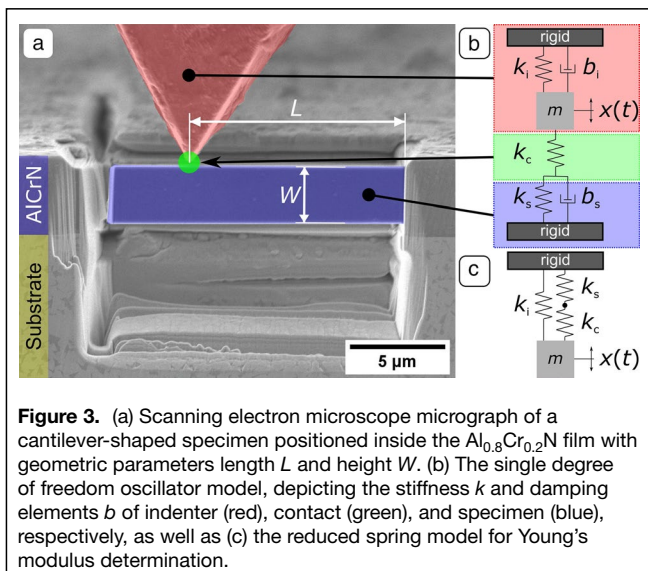

Figure 2. X-ray diffraction data of the thin-film samples in as-deposited (blue) and heat-treated (red) states, respectively. The inset details the 200 peak of cubic CrN, showing evident increase of this phase upon annealing.

are gathered by fitting the resonance peak based on a physical single degree of freedom (SDOF) oscillator model, as shown schematically in Figure 3b using the lmfit package (version 1.0.0) within the Python 3.8 programming environment.[27]

Initial data are gathered as dynamic compliance c for the whole system as a function of frequency, whereby $c(\omega) = \Delta x(\omega)/\Delta F$, with displacement amplitude Δx and load amplitude ΔF. To compare the specimens among themselves, it is useful to normalize the radial frequency by the resonance frequency $\omega_0 = \sqrt{k/m}$ and the compliance by the static compliance $c_0(\omega = 0) = 1/k$, with mass m and stiffness k. The resulting data are summarized in **Figure 4**, wherein the as-deposited specimens are depicted by open symbols and the heat-treated ones are indicated by filled symbols. The damping capability of a material is commonly quantified as inverse quality factor Q^{-1}, which is the ratio between dissipated work ΔW and total conducted work W during one oscillation cycle and can be written as:

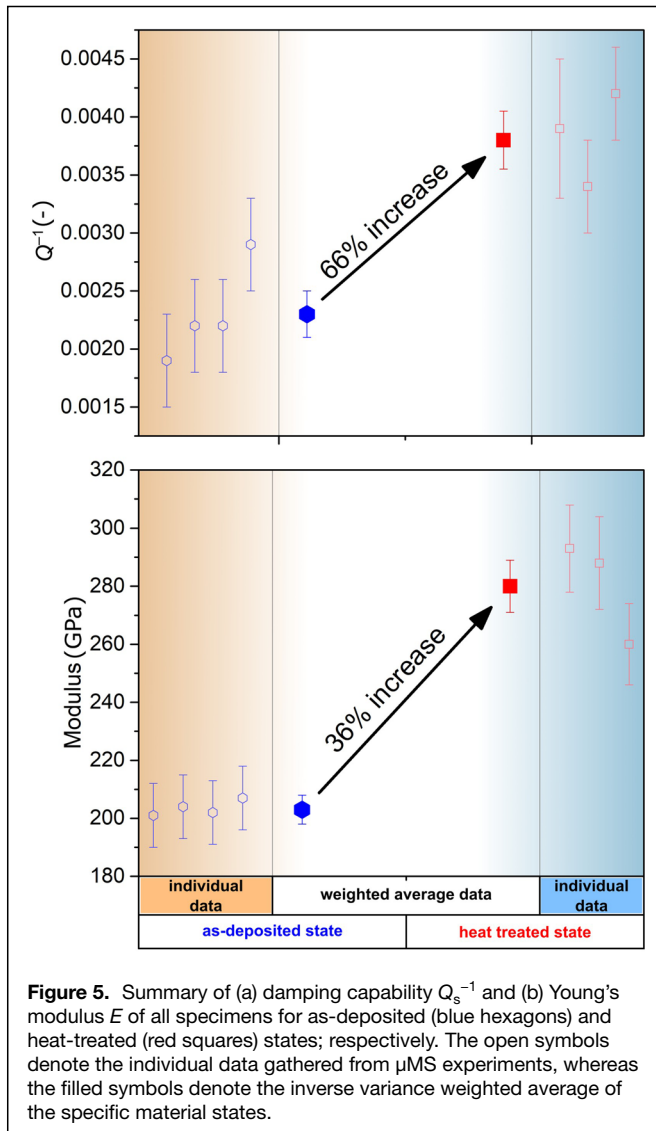$$Q^{-1} = \frac{\Delta W}{2\pi W} = \frac{b}{\sqrt{km}} \qquad 1$$

with the viscous damping constant b. In Figure 4 the average resonance curve for all as-deposited specimens ($Q_{ad}^{-1} = 1.06 \times 10^{-2} \pm 1 \times 10^{-4}$) is depicted with a blue solid line and the average resonance curve for all heat-treated specimens ($Q_{ht}^{-1} = 1.124 \times 10^{-2} \pm 1 \times 10^{-4}$) is given by a dashed red line. As the damping of the system is large in comparison to that of the individual cantilevers, observing the difference is rather challenging in the whole data graph. Therefore, the yellow inset in Figure 4 (top right corner) details the peak tip region and shows the evident difference in peak height for the two specimen states. Furthermore, all of the as-deposited states show a very distinct damping peak on the right-hand side of the main resonance peak at an absolute average radial frequency position of $\omega = 1849 \pm 4$ Hz, which is not evident in the heat-treated specimens. These peaks are shown as detailed inset

Figure 4. Resonance peaks of all tested specimens, normalized by resonance frequency ω_0 and static compliance of the total system c_{total} ($\omega = 0$). The as-deposited specimens are denoted by open symbols and the heat treated by filled symbols, respectively. The solid blue line represents the average resonance shape of the whole system for all as-deposited data with $Q^{-1} = 0.0106$, whereas the dashed red line represents the same for all heat-treated data with $Q^{-1} = 0.0124$. Two insets show details of the resonance peak for both states and an occurring damping peak in as-deposited state at higher resolution, respectively.

Figure 3. (a) Scanning electron microscope micrograph of a cantilever-shaped specimen positioned inside the $Al_{0.8}Cr_{0.2}N$ film with geometric parameters length L and height W. (b) The single degree of freedom oscillator model, depicting the stiffness k and damping elements b of indenter (red), contact (green), and specimen (blue), respectively, as well as (c) the reduced spring model for Young's modulus determination.

in Figure 4 (lower right corner). Note that those are slightly shifted among themselves as the resonance frequency of the individual cantilevers is not identical due to minor geometrical variations.

To obtain the damping capability of the material system independent of the probing indenter one needs to take into account the work that is dissipated by the indenter system out of contact (i.e., $Q_s^{-1} = Q^{-1} - Q_i^{-1}$), whereby the subscripts s and i denote the specimen and indenter, respectively. The individual specimen inverse quality factor Q_s^{-1} is summarized in **Figure 5**a, where the data for each as-deposited cantilever are depicted by open blue hexagons (left-hand side) and that for each heat-treated cantilever by open red squares (right-hand side). All uncertainty estimates are considered based on uncorrelated input quantities[31] with geometric measurement errors of ± 3 px (± 50 nm) and all parameter errors taken as one standard deviation, given by the fitting procedure. The filled data points in Figure 5 depict the inverse variance weighted average of all individual µMS experiments for the two respective material states. There the error bars denote the standard error of the weighted average. From Figure 5a it is evident that the damping capability increases quite significantly by about 66% from $Q_{s,ad}^{-1} = 2.3 \times 10^{-3} \pm 2 \times 10^{-4}$ for the as-deposited state to $Q_{s,ht}^{-1} = 3.8 \times 10^{-3} \pm 3 \times 10^{-4}$ for the heat-treated state, respectively.

Furthermore, µMS experiments allow for the determination of Young's modulus based on the frequency shift of the peak, as this corresponds to the cantilever specimen stiffness k_s. However, to determine the individual specimen's stiffness from the total stiffness k without the contributions of the indenter system

Figure 5. Summary of (a) damping capability Q_s^{-1} and (b) Young's modulus E of all specimens for as-deposited (blue hexagons) and heat-treated (red squares) states; respectively. The open symbols denote the individual data gathered from μMS experiments, whereas the filled symbols denote the inverse variance weighted average of the specific material states.

and the contact between tip and specimen surface, one needs to consider a reduced model as shown in Figure 3c, where the specimen stiffness k_s and contact stiffness k_c are series-connected and the indenter stiffness k_i is in parallel to both of them. This is due to the fact that both the specimen and the indenter tip are connected with the rigid base inside the SEM, giving them a common ground in analogy to electric circuits. The specimen stiffness k_s is calculated as follows:

$$k_s = \left(\frac{1}{k - k_i} - \frac{1}{k_c} \right)^{-1}. \qquad 2$$

While the indenter stiffness is obtained during the calibration routine of the instrument, the contact stiffness is a function of the contact force and needs to be measured on the base of the cantilever.[32] For the given experiments at an average constant contact force of 500 μN a contact stiffness of $k_c = 44{,}030$ N/m was determined. Using the fact that during the experiment only small total load line displacements of

≈250 nm, leading to small rotation angles of ≈1.5°, are used, one can utilize the simple Euler–Bernoulli beam theory[33] to calculate the Young's modulus E as:

$$E = \frac{4k_s L^3}{BW^3}. \qquad 3$$

The data are summarized in Figure 5b, where the same color scheme and uncertainty propagation calculations as for the Q^{-1} data are employed. It is evident that the modulus increases by about 36% from $E_{ad} = 205 \pm 6$ to $E_{ht} = 280 \pm 9$ GPa, from the as-deposited to the heat-treated states, respectively.

Discussion

The discussion will be structured into sections regarding phase formation, change in damping capability and increase in modulus, respectively.

Cubic CrN phase formation

The evident phase formation of the cubic CrN phase after annealing, as detailed in a recent previous work on a similar composition $(Al_{0.9}Cr_{0.1}N)$,[17] is driven by the supersaturation of Cr atoms inside the equilibrium AlN crystal structure as a mainly wurtzite type $Al_{0.8}Cr_{0.2}N$ solid solution (Figure 2).

To estimate the amount of cubic CrN phase that forms upon annealing, Rietveld refinement (PowderCell 2.4[34]) was used on the data presented in Figure 2, utilizing the actual crystallographic spacing of the similar supersaturated wurtzite $Al_{0.9}Cr_{0.1}N$ structure ($a = 313.3$ pm, $c = 500.3$ pm[17]) as initiation parameters. After subtraction of the distinct peaks of the TiN bonding layer and the WC substrate the contents of the wurzite-type matrix structure compute to 94 and 85%, while the cubic CrN contents enumerate to 6 and 15% for the as-deposited and heat-treated material states, respectively. This suggests that already in the as-deposited state a minor amount of cubic CrN is present, but upon annealing the amount increases by about 9 percent. As the microstructure is rather homogeneous in the as-deposited state (Figure 1c), these microstructural regions seem to be below the resolution limit of the gathered STEM images, so in the range of a few nanometers. Furthermore, the fact that only 15% CrN is evident after annealing suggests that still about 5% of Cr remain incorporated inside the wurtzite AlN matrix, as the driving force for the Cr to diffuse out is reduced by the relaxation of eigenstresses, due to defect annihilation and segregation as evident from the AlN peak shift (Figure 2). As complementary analysis, multiple STEM micrographs of the heat-treated state (similar to Figure 1d) have been analyzed by image thresholding (ImageJ 1.54s[35]) using manual threshold inputs to obtain estimates for the area fraction of the CrN phase. The results ranged from approximately 5 to 16%, which includes the influence of human input parameters as well as locally different CrN content that could occur due to the stochastic distribution of Cr. However, these values show reasonable agreement with

the Rietveld analysis and corroborate that the major amount of cubic CrN forms these evident approximately 10–20-nm-sized precipitates.

Elastic modulus change

The elastic modulus of the as-deposited mainly wurtzite $Al_{0.8}Cr_{0.2}N$ is considerably lower at 205 ± 6 GPa than the elastic modulus of pure wurtzite AlN would be with ~ 301 GPa[36] (calculated by the Voigt–Reuss–Hill (VRH) approximation[37,38]) from simulations or ~340 GPa[39] from experimental measurements. One could argue that this decrease of elastic modulus is a result of the larger unit cell given the Cr incorporation. Using the proportionality relations between elastic modulus E, bulk modulus K, and the second derivative of the binding energy over unit cell volume $\frac{\partial^2 U}{\partial V^2}$, as commonly described by the Birch–Murnaghan equation of state,[40,41] in conjunction with the difference between supersaturated and relaxed unit cell size from Meindlhumer et al.[17] (roughly 0.5%), it is possible to estimate the change of elastic modulus to be approximately 2 percent. This would mean the modulus change based on the increased unit cell size in the as-deposited $Al_{0.8}Cr_{0.2}N$ in comparison to the equilibrium AlN, would amount to only about 6 GPa (from 301 to 295 GPa), which seems not enough of a difference to explain the discrepancy observed herein. However, considering on the other hand the fact that Cr is most likely substitutional on Al positions within the wurtzite structure, one can argue that the change in bonding energy between the species could alter the elastic response. Although the precise bonding energies of the individual species combinations inside the crystal structure are near impossible to obtain, binding energies of two-atomic structures are tabulated and can act as a first-order estimate.[42] The strengths of either Al–N bonds (3.81 eV) and Cr–N bonds (3.92 eV) differ only slightly by about 3%, whereas the Al–Al bonds (2.74 eV) are significantly stronger than the Al–Cr bonds (2.31 eV) by about 16 percent. As the elastic properties of crystals are a direct result of the bonding strengths, this could act as a source for the reduced modulus given the forced incorporation of Cr within the wurtzite AlN structure. Considering now the heat-treated specimens suggests two possible sources for an increased modulus. First the precipitation of larger cubic CrN regions with an inherently higher elastic modulus of 358 GPa[43] (using again the VRH approximation[37,38]), or second the statistical increase in stronger Al–Al bonds, within the wurtzite $Al_xCr_{1-x}N$ structure, due to dissolution of the Cr out of the matrix.

The initial elastic modulus in the as-deposited $Al_{0.8}Cr_{0.2}N$ is also in good agreement with the single-crystal *ab initio* calculations by Mayrhofer et al.,[44] who found elastic moduli ranging from 188 to 195 GPa for the wurtzite $Al_xCr_{1-x}N$ system, respectively.

To validate the present results, nanoindentation experiments were performed on the films without any prior surface preparation. As nanoindentation experiments only determine a reduced modulus, they are not directly comparable to the µMS results

as these determine the actual material's elastic modulus. Therefore, the Poisson's ratio for AlN $v=0.24$ was assumed to calculate the material's indentation moduli as $E_{i,ad}=266\pm34$ GPa and $E_{i,ht}=326\pm82$ GPa for the as-deposited and heat-treated states, respectively. While a similar trend of modulus increase is evident in the nanoindentation data, the rough surface of the unpolished films as well as the unknown microstructural features underneath the indents (e.g., droplets [see Figure 1c]) lead to a rather large scatter in comparison with the µMS results. One could improve the nanoindentation results by prior polishing steps. However, given that the system is only 6 µm in thickness and a certain thickness must be retained for nanoindentation to determine a substrate-influence free modulus, this could be rather challenging. Similar limitations apply to a cross-sectional approach.[45] Therefore, it appears that although the preparation via FIB milling is more cumbersome, the modulus determination using µMS could be beneficial in systems with a high surface roughness or small geometric spacing, such as the $Al_{0.8}Cr_{0.2}N$ layer as studied herein. Furthermore, the fact that no initial Poisson's ratio estimate is necessary means that unknown changes in this ratio upon precipitation or other microstructural changes have no influence on the final result.

Change in damping capabilities

Commonly the damping capability is reduced after annealing as dissipative elements such as residual defects are either removed (e.g., dislocations,[46] vacancies)[47] or relaxed (e.g., grain boundaries).[27,48,49] Therefore, the present increase of damping by about 66% upon annealing seems rather counterintuitive. Especially, considering the small damping peak at $\omega=1849\pm4$ Hz in the as-deposited state, which is not apparent after heat treatment suggests that some easy to activate anelastic relaxation processes were removed (e.g., annealing of defects from a metastable, to a more stable (equilibrium) state took place). Independent of the actual underlying process, these peaks are known to follow an Arrhenius relationship,[50,51] as:

$$t = t_0 e^{\frac{H}{kT}}, \qquad\qquad 4$$

where t, t_0 are the relaxation time and limit relaxation time, H is an activation enthalpy, k is the Boltzmann constant, and T is the temperature. While classical internal friction experiments change temperature as well as frequency to measure t_0 and H, one can use the inverse of the Debye frequency of wurtzite AlN as $t_0 \approx 10^{-13}-10^{-15}$ [52,53] to obtain a first-order approximation for H. In conjunction with the constant room temperature $T = 22°C$ (air conditioned), the activation enthalpy for a peak with a relaxation time of $t = 0\omega^{-1}$ s, equates to $H \approx 0.57 - 0.69$ eV. Commonly, crystalline dissipative mechanisms can be separated into three main categories, namely short-range diffusion, for example, Snoek relaxation,[54] dislocation-based mechanisms,[55–57] or grain-boundary (phase boundary)-based mechanisms.[58–60] Considering that any type of oscillatory dislocation motion in this hard nanoceramic coating is unlikely to occur under the small load amplitude of 5 µN, which corresponds to a maximum stress

amplitude of approximately 10 MPa at the base of the cantilever, this mechanism can be neglected.

If bulk diffusion processes would have a major contribution to the damping peak, the estimated activation enthalpy should agree with activation energies for the corresponding diffusional process.

Density functional theory calculations of vacancy diffusion within wurtzite AlN suggest an activation energy of approximately 2.33 eV[61] and Okumura et al.[62] measured the activation energy for impurity diffusion (Si and O) within wurtzite AlN as approximately 1.3 eV using positron annihilation. None of these energies are low enough to be comparable with the estimate of 0.57–0.69 eV from the observed damping peak. Therefore, the processes correlated with this damping peak most likely results of the nonequilibrium crystal structure in the as-deposited state (i.e., metastable atom positions due to the forced incorporation of Cr or very small local wurtzite-cubic structural interfaces that are already present), as suggested by the XRD data (Figure 2). This is further supported by the fact that vacancy formation energies seem to be generally reduced in unrelaxed (i.e., deformed), in comparison to the relaxed (i.e., annealed state in (Ti,Al)N/AlN interfaces), as reported from *ab initio* simulations.[63]

The disappearance of this small peak upon annealing would imply a lower amount of dissipating processes, and if the processes corresponding to this peak would contribute to the overall damping in a major extent, also the main resonance damping peak should decrease, leading to a lower Q^{-1} in the heat-treated state.

However, the observed precipitation of the CrN phase results in an increase in phase boundary area, which can also contribute to the damping capability of the system. Schoeck[64] derived an analytical expression for the change in Q^{-1} upon precipitation based on the shape change, elastic modulus mismatch, and occurrence of incoherent phase boundaries, respectively. He argued that the first two cases seem unreasonable due to the fact that a change in shape would need to incorporate some kind of diffusional component for anelastic relaxation to occur, and a mismatch in elastic modulus leads to instantaneous changes (no time dependence—therefore no anelastic relaxation) upon load reversal, leaving only relaxation processes within incoherent boundaries as reasonable sources for damping. His treatment was based on a quasi-degenerate ellipsoidal regime with half-axis a, which contains the incoherent boundary and leads to:

$$Q^{-1} = \frac{1}{\tau^2}\frac{8(1-\nu)}{3\pi(2-\nu)}\frac{\sum_i a_i^3 \tau_i^2}{V} \approx 0.0194 \frac{V_{\text{precipitates}}}{V}, \quad 5$$

where τ, τ_i are a global homogeneous and a local acting shear stress, respectively, and V is the total specimen volume. This rather abstract geometrical description is challenging to correlate with experimental data. Idealizing the system by assuming that the homogeneous global shear stress is rather a shear stress distribution being equal to the shear stress distribution acting on the interfaces removes τ and τ_i from the equation.

Furthermore, assuming that all precipitates are dodecahedral in shape and are of the same size allows to establish a relationship between the elliptical half-axis a and the (average) precipitate volume $V_{\text{precipitates}}$, by setting the cross-sectional area of the ellipsoid and one of the 12 sides' areas of the dodecahedron to be equal, as schematically depicted in **Figure** 6a. Based on this simplified system one can estimate the increase in volume fraction of precipitates within the specimen based on the change in damping capability ($\Delta Q^{-1} \approx 1.5 \times 10^{-3}$) to be approximately 7.7%, which agrees convincingly well with the increase of the cubic CrN phase deduced from Rietveld analysis (9%), and suggests that the dissipating processes within incoherent interfaces have a major contribution to the observed damping increase upon annealing. Similar behavior has been previously observed only in metallic systems (Ni–Al,[65] Cu–O,[66] Al–Cu,[67] Al–Mg[68]), where semi-coherent or incoherent precipitation formation lead to the occurrence of a temperature independent relaxation peak in internal friction experiments.

Although it is generally not known whether cubic CrN precipitates form completely incoherently within the wurtzite AlN matrix, the precipitates that form on grain boundaries will most likely have at least one incoherent interface, as it will be nearly impossible to exhibit two (or more—considering triple junctions) coherent interfaces during formation between two randomly oriented grains. This is shown representatively in the high-resolution TEM micrograph in Figure 6b, where a CrN precipitate with two distinctly different crystal orientations on either side (upper, lower) is depicted. The lower boundary is detailed in Figure 6c, with the zoomed region on the left-hand side and the corresponding Fourier-filtered image (using only the first-order peaks) on the right-hand side. There, the continuation of the lattice planes as evidenced in the Fourier-filtered image demonstrates coherency between the precipitate and the matrix. In Figure 6d, a same-sized region of the upper boundary as well as the corresponding Fourier-filtered image are depicted. While the complete three-dimensional structure of the boundary is not resolvable, the evident loss of coherency in the image suggests an incoherent boundary. This, in conjunction with the arguable absence of other major dissipative mechanisms makes anelastic relaxation within incoherent cubic CrN–wurtzite AlN boundaries the most likely mechanism for the observed increase in overall damping capacity.

Although this novel methodology probes a rather wide ensemble of inherent defects, the analysis and separation of these individual defects' structures is not straightforward. For chemically simpler materials (i.e., single species), an attempt to match the obtained Q^{-1} values to different defect types could be the correlative molecular dynamics approach[69] where individual defects (dislocations, vacancy clusters, GBs) under load result in varying phase shifts between shear stress and strain, which can be directly correlated to damping magnitude.
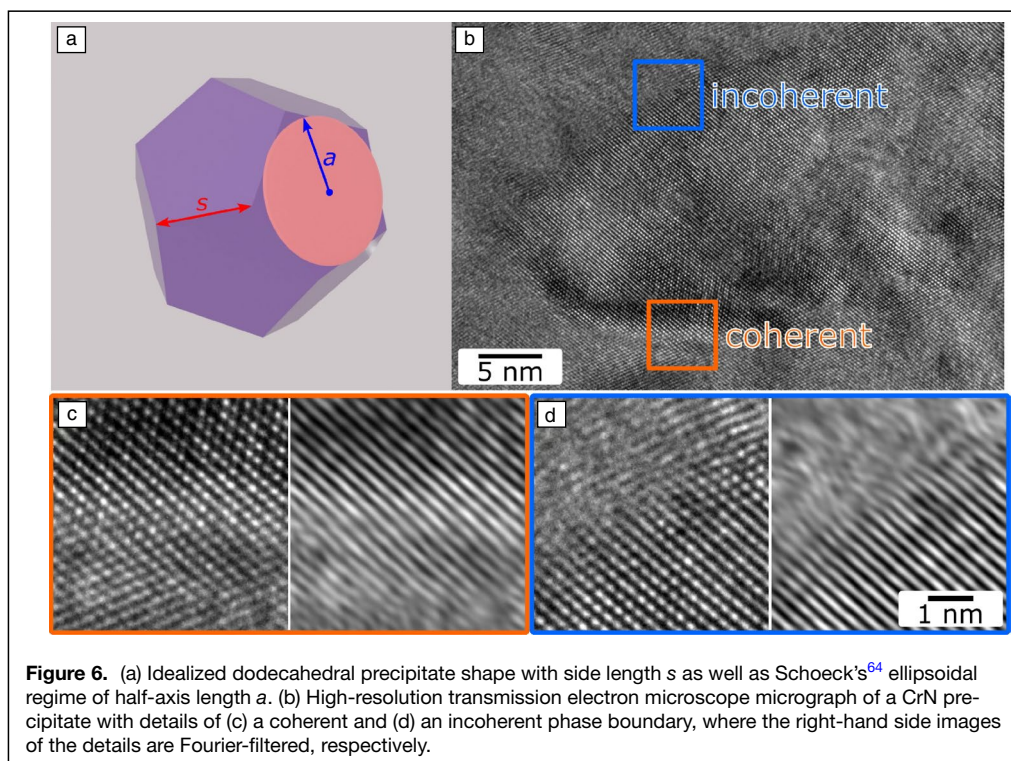
Figure 6. (a) Idealized dodecahedral precipitate shape with side length *s* as well as Schoeck's[64] ellipsoidal regime of half-axis length *a*. (b) High-resolution transmission electron microscope micrograph of a CrN precipitate with details of (c) a coherent and (d) an incoherent phase boundary, where the right-hand side images of the details are Fourier-filtered, respectively.

it underlines that the novel µMS methodology is able to resolve microstructural changes, even in the grain/phase boundary regime of very confined volumes of only a few micrometers. This makes it a useful complementary technique to bridge the gap between high-resolution single-boundary investigations (i.e., by TEM and macroscopic investigations on the whole device).

Materials and methods

Thin-film deposition and heat treatment

The initial $Al_{0.8}Cr_{0.2}N$ thin films were deposited on a cemented carbide (WC, 10 wt% Co) substrates by cathodic arc evaporation (alpha 400p, voestalpine eifeler Vacotec GmbH, Düsseldorf, Germany) at a bias voltage of $U_B = -100$ V, substrate temperature $T_s = 475°C$, and nitrogen pressure $p_{N2} = 4$ Pa. The $10 \times 10 \times 5$ mm^3 mirror-polished cemented carbide substrates were mounted at a distance of ~100 mm from the cathodes in a onefold rotation holder operated at a speed of 2 rpm and were plasma cleaned before deposition. First, a ~200-nm TiN bonding layer was deposited utilizing a single Ti cathode to inhibit diffusion between substrate and film during annealing followed by $Al_{0.8}Cr_{0.2}N$ deposited from five sintered $Al_{0.8}Cr_{0.2}$ cathodes. The same deposition conditions were used throughout the whole deposition process. The final film thickness was measured using SEM to be ~6 µm.

To obtain microstructural changes individual samples were annealed for 5 min at 1050°C in a vacuum atmosphere ($p_{anneal} = 5 \times 10^{-4}$ Pa) using a conventional high vacuum furnace (HTM Reetz GmbH, Berlin, Germany) operated at heating and cooling rates of 0.5 K/s.

Electron microscopy and x-ray diffraction

Microstructural investigations were conducted using an SEM (Leo 1525, Carl Zeiss AG, Oberkochen, Germany) operated at 3 kV using secondary electron as well as backscatter electron imaging. Furthermore, electron transparent foils of the film cross section were prepared via focused ion beam milling (FIB, Helios NanoLab 660, Thermo Fisher Scientific Inc., Waltham, Mass., USA) and analyzed using a TEM (Titan Themis, Thermo Fischer Scientific Inc., Waltham, Mass.,

Summary and conclusion

In the present work an $Al_{0.8}Cr_{0.2}N$ thin film of about 6-µm thickness was deposited on cemented carbide by cathodic arc evaporation as commonly found in commercially available high-speed dry-milling tools. A heat treatment of 1050°C for only 5 min led to the formation of cubic CrN precipitates within the otherwise wurtzite Al(Cr)N matrix, as evidenced by TEM and XRD investigations. The dynamic-mechanical properties of the film in both material states, as-deposited and heat-treated, were investigated using the novel µMS methodology and revealed an increase of Young's modulus by about 36% from $E_{ad} = 205 \pm 6$ GPa to $E_{ht} = 280 \pm 9$ GPa, as well as an increase in damping capability of about 66%, from $Q_{s,ad}^{-1} = 2.3 \times 10^{-3} \pm 2 \times 10^{-4}$ to $Q_{s,ht}^{-1} = 3.8 \times 10^{-3} \pm 3 \times 10^{-4}$, upon annealing. The modulus from µMS experiments is in agreement to theoretical and experimental literature values, as well as nanoindentation results, which validates the new methodology. The lower scatter of the µMS results (approximately 3%) in comparison to the nanoindentation data (up to 25%), suggests that this technique could be beneficial in systems with high surface roughness and/or a limited spatial extent, such as the thin-film system studied herein. Furthermore, the evaluation is independent of the oftentimes unknown Poisson's ratio. The increase in damping upon annealing is most likely a result of the formation of incoherent phase boundaries between the cubic CrN precipitates and the wurtzite Al(Cr)N matrix. This previously unresolvable increase in damping can be beneficial considering the application for high-speed dry milling, as it detains mechanical vibration and therefore stress spikes, which can lead to fracture of the hard coating. Furthermore,

USA) operated at 200 kV accelerating voltage and a probe current of 1 nA equipped with a detector for energy-dispersive spectroscopy (ChemiSTEM Super-X spectrometer, Thermo Fisher Scientific Inc., Waltham, Mass., USA) to obtain local chemical information. XRD phase analysis of the samples was performed using a five-circle x-ray diffractometer (SmartLab, Rigaku Co., Tokyo, Japan) equipped with Cu–Kα radiation, a parabolic multilayer mirror in the primary beam, and a secondary graphite monochromator. The XRD characterization was carried out in grazing incidence geometry with 5° incidence angle.

Nanoindentation and micromechanical spectroscopy

Nanoindentation experiments were conducted on both material states without prior surface preparation using a G200 Nanoindenter (KLA Corporation, Milpitas, Calif., USA) with a diamond Berkovich tip. Depth-sensitive hardness and reduced modulus were gathered using continuous stiffness measurement at a frequency of 45 Hz, a loading rate of 0.05 s^{-1}, and was averaged between 170- and 190-nm penetration depth.

Micromechanical spectroscopy was conducted following the procedure developed in previous works[27] on cantilever-shaped specimens with a geometry of ~2 × 3 × 12 μm^3 processed by FIB (1540XB, Carl Zeiss AG, Oberkochen, Germany) operated at 30 kV and with subsequently reducing currents from 10 nA to 50 pA. The experiments were conducted using a Hysitron PI85 (Bruker Corporation, Billerica, Mass., USA) transducer with a nanoDMA III upgrade, which exhibits an inherent resonance frequency at 114 Hz, and was equipped with a 5-μm-wide conductive diamond wedge tip (Synton-MDP AG, Nidau, Switzerland). The specimens were loaded to a contact force of 500 μN and the oscillation amplitude was kept constant at 5 μN, while the frequency sweep was conducted from 200 to 300 Hz with a randomized frequency pattern and three repetitions with differing frequency spacing for reproducibility checks and to obtain a higher resolution toward the contact resonance peak. The combined tip and shaft mass as well as the indenter stiffness were measured during the usual calibration routine as $m = 805.63$ mg and $k_i = 419.62$ N/m, respectively, and the inherent damping of the indenter is $Q^{-1}_i = 8.34 \times 10^{-3} \pm 3.7 \times 10^{-4}$.

Acknowledgments

Funding

Data availability

The raw/processed data required to reproduce these findings are available from the corresponding author upon reasonable request.

Conflict of interest

On behalf of all authors, the corresponding author states that there is no conflict of interest.

Open access

References

1. P.H. Mayrhofer, C. Mitterer, L. Hultman, H. Clemens, *Prog. Mater. Sci.* **51**, 1032 (2006). https://doi.org/10.1016/j.pmatsci.2006.02.002
2. C. Mitterer, *Comprehensive Hard Materials* (Elsevier, Amsterdam, 2014), vol. 2, p. 449. https://doi.org/10.1016/B978-0-08-096527-7.00035-0.
3. J.G. Thakare, C. Pandey, M.M. Mahapatra, R.S. Mulik, *Met. Mater. Int.* **27**, 1947 (2020). https://doi.org/10.1007/s12540-020-00705-w
4. A.G. Evans, D.R. Mumm, J.W. Hutchinson, G.H. Meier, F.S. Pettit, *Prog. Mater. Sci.* **46**, 505 (2001). https://doi.org/10.1016/S0079-6425(00)00020-7
5. M.R. Begley, H.N.G. Wadley, *Acta Mater.* **60**, 2497 (2012). https://doi.org/10.1016/j.actamat.2011.12.039
6. J. Vetter, *Surf. Coat. Technol.* **76–77**, 719 (1995). https://doi.org/10.1016/0257-8972(95)02499-9
7. M. Kawate, A.K. Hashimoto, T. Suzuki, *Surf. Coat. Technol.* **165**, 163 (2003). https://doi.org/10.1016/S0257-8972(02)00473-5
8. M. Kawate, A. Kimura, T. Suzuki, *J. Vac. Sci. Technol. A* **20**(2), 569 (2002). https://doi.org/10.1116/1.1448510
9. A.E. Reiter, V.H. Derflinger, B. Hanselmann, T. Bachmann, B. Sartory, *Surf. Coat. Technol.* **200**, 2114 (2005). https://doi.org/10.1016/j.surfcoat.2005.01.043
10. M. Meindlhumer, S. Klima, N. Jäger, A. Stark, H. Hruby, C. Mitterer, J. Keckes, R. Daniel, *Sci. Rep.* **9**, 18027 (2019). https://doi.org/10.1038/s41598-019-54307-7
11. L. Rogström, J. Ullbrand, J. Almer, L. Hultman, B. Jansson, M. Odén, *Thin Solid Films* **520**, 5542 (2012). https://doi.org/10.1016/j.tsf.2012.04.059
12. P.H. Mayrhofer, A. Hörling, L. Karlsson, J. Sjölén, T. Larsson, C. Mitterer, L. Hultman, *Appl. Phys. Lett.* **83**, 2049 (2003). https://doi.org/10.1063/1.1608464
13. M. Bartosik, C. Rumeau, R. Hahn, Z.L. Zhang, P.H. Mayrhofer, *Sci. Rep.* **7**, 16476 (2017). https://doi.org/10.1038/s41598-017-16751-1
14. L. Chen, J. Paulitsch, Y. Du, P.H. Mayrhofer, *Surf. Coat. Technol.* **206**, 2954 (2012). https://doi.org/10.1016/j.surfcoat.2011.12.028
15. H. Willmann, P.H. Mayrhofer, P.O.Å. Persson, A.E. Reiter, L. Hultman, C. Mitterer, *Scr. Mater.* **54**, 1847 (2006). https://doi.org/10.1016/j.scriptamat.2006.02.023
16. P.H. Mayrhofer, H. Willmann, A.E. Reiter, *Surf. Coat. Technol.* **202**, 4935 (2008). https://doi.org/10.1016/j.surfcoat.2008.04.075
17. M. Meindlhumer, T. Ziegelwanger, J. Zalesak, M. Hans, L. Löfler, S. Spor, N. Jäger, A. Stark, H. Hruby, R. Daniel, D. Holec, J.M. Schneider, C. Mitterer, J. Keckes, *Acta Mater.* **237**, 118156 (2022). https://doi.org/10.1016/j.actamat.2022.118156
18. S.J. Bull, *J. Phys. D Appl. Phys.* **38**(24), R393 (2005). https://doi.org/10.1088/0022-3727/38/24/R01

19. M. Sebastiani, K.E. Johanns, E.G. Herbert, F. Carassiti, G.M. Pharr, *Philos. Mag.* **95**, 1928 (2015). https://doi.org/10.1080/14786435.2014.913110

20. A. Riedl, R. Daniel, M. Stefenelli, T. Schöberl, O. Kolednik, C. Mitterer, J. Keckes, *Scr. Mater.* **67**, 708 (2012). https://doi.org/10.1016/j.scriptamat.2012.06.034

21. M. Sebastiani, C. Eberl, E. Bemporad, G.M. Pharr, *Mater. Sci. Eng. A* **528**(27), 7901 (2011). https://doi.org/10.1016/j.msea.2011.07.001

22. S. Massl, J. Keckes, R. Pippan, *Acta Mater.* **55**, 4835 (2007). https://doi.org/10.1016/j.actamat.2007.05.002

23. R. Treml, D. Kozic, J. Zechner, X. Maeder, B. Sartory, H.P. Gänser, R. Schöngrundner, J. Michler, R. Brunner, D. Kiener, *Acta Mater.* **103**, 616 (2016). https://doi.org/10.1016/j.actamat.2015.10.044

24. M. Stefenelli, J. Todt, A. Riedl, W. Ecker, T. Müller, R. Daniel, M. Burghammer, J. Keckes, *J. Appl. Crystallogr.* **46**, 1378 (2013). https://doi.org/10.1107/S0021889813019535

25. M. Meindlhumer, N. Jäger, S. Spor, M. Rosenthal, J.F. Keckes, H. Hruby, C. Mitterer, R. Daniel, J. Keckes, J. Todt, *Scr. Mater.* **182**, 11 (2020). https://doi.org/10.1016/j.scriptamat.2020.02.031

26. M. Meindlhumer, L.R. Brandt, J. Zalesak, M. Rosenthal, H. Hruby, J. Kopecek, E. Salvati, C. Mitterer, R. Daniel, J. Todt, J. Keckes, A.M. Korsunsky, *Mater. Des.* **198**, 109365 (2021). https://doi.org/10.1016/j.matdes.2020.109365

27. M. Alfreider, I. Issa, O. Renk, D. Kiener, *Acta Mater.* **185**, 309 (2020). https://doi.org/10.1016/j.actamat.2019.12.011

28. A.O. Eriksson, J.Q. Zhu, N. Ghafoor, M.P. Johansson, J. Sjölen, J. Jensen, M. Odén, L. Hultman, J. Rosén, *Surf. Coat. Technol.* **205**(15), 3923 (2011). https://doi.org/10.1016/j.surfcoat.2011.02.007

29. M. Hans, M. to Baben, Y.-T. Chen, K.G. Pradeep, D.M. Holzapfel, D. Primetzhofer, D. Kurapov, J. Ramm, M. Arndt, H. Rudigier, J.M. Schneider, *Surf. Coat. Technol.* **305**, 249 (2016). https://doi.org/10.1016/j.surfcoat.2016.08.046

30. S. Gleich, R. Soler, H. Fager, H. Bolvardi, J.-O. Achenbach, M. Hans, D. Primetzhofer, J.M. Schneider, G. Dehm, C. Scheu, *Mater. Des.* **142**, 203 (2018). https://doi.org/10.1016/j.matdes.2018.01.029

31. International Organization for Standardization/International Electrotechnical Commission (ISO/IEC), *Uncertainty of Measurement—Part 3: Guide to the Expression of Uncertainty in Measurement (GUM:1995)* (ISO/IEC Guide 98-3, 2008)

32. M. Alfreider, D. Kozic, O. Kolednik, D. Kiener, *Mater. Des.* **148**, 177 (2018). https://doi.org/10.1016/j.matdes.2018.03.051

33. J.M. Gere, S.P. Timoshenko, *Mechanics of Materials* (Springer, New York, 2013). https://doi.org/10.1007/978-1-4899-3124-5

34. W. Kraus, G. Nolze, *J. Appl. Crystallogr.* **29**, 301 (1996). https://doi.org/10.1107/S0021889895014920

35. C.A. Schneider, W.S. Rasband, K.W. Eliceiri, *Nat. Methods* **9**, 671 (2012). https://doi.org/10.1038/nmeth.2089

36. A.J. Wang, S.L. Shang, Y. Du, Y. Kong, L.J. Zhang, L. Chen, D.D. Zhao, Z.K. Liu, *Comput. Mater. Sci.* **48**, 705 (2010). https://doi.org/10.1016/j.commatsci.2010.03.014

37. R. Hill, *Proc. Phys. Soc. A* **65**(5), 349 (1952). https://doi.org/10.1088/0370-1298/65/5/307

38. J.P. Watt, G.F. Davies, R.J. O'Connell, "The Elastic Properties of Composite Materials," in *Elastic Properties and Equations of State*, vol. 26, ed. by T.J. Shankland, J.D. Bass (American Geophysical Union, Washington, DC, 1988), p. 384. https://doi.org/10.1029/SP026p0384

39. E. Österlund, J. Kinnunen, V. Rontu, A. Torkkeli, M. Paulasto-Kröckel, *J. Alloys Compd.* **772**, 306 (2019). https://doi.org/10.1016/j.jallcom.2018.09.062

40. S.L. Shang, Y. Wang, D.E. Kim, Z.K. Liu, *Comput. Mater. Sci.* **47**, 1040 (2010). https://doi.org/10.1016/j.commatsci.2009.12.006

41. Z. Liu, J. Shang, *Rare Metals* **30**, 354 (2011). https://doi.org/10.1007/s12598-011-0302-9

42. Y.-R. Luo, *Comprehensive Handbook of Chemical Bond Energies* (CRC Press, Boca Raton, 2007). https://doi.org/10.1201/9781420007282

43. L. Löfler, R. Hahn, P.H. Mayrhofer, M. Bartosik, D. Holec, *Acta Mater.* **218**, 117095 (2021). https://doi.org/10.1016/j.actamat.2021.117095

44. P.H. Mayrhofer, D. Music, T. Reeswinkel, H.-G. Fuß, J.M. Schneider, *Acta Mater.* **56**(11), 2469 (2008). https://doi.org/10.1016/j.actamat.2008.01.054

45. D. Kiener, A.M. Minor, O. Anderoglu, Y. Wang, S.A. Maloy, P. Hosemann, *J. Mater. Res.* **27**, 2724 (2012). https://doi.org/10.1557/jmr.2012.303

46. A. Rivière, M. Gerland, V. Pelosin, *Mater. Sci. Eng. A* **521**, 94 (2009). https://doi.org/10.1016/j.msea.2008.09.100

47. I.S. Golovin, S. Jäger, V.A. Semin, G.V. Serzhantova, H.R. Sinning, O.A. Sokolova, F. Stein, S.A. Golovin, *Solid State Phenom.* **137**, 69 (2008). https://doi.org/10.4028/www.scientific.net/SSP.137.69

48. I.S. Golovin, P.P. Pal-Val, L.N. Pal-Val, E.N. Vatazhuk, Y. Estrin, *Solid State Phenom.* **184**, 289 (2012). https://doi.org/10.4028/www.scientific.net/SSP.184.289

49. F.-C. Hsu, Y.-T. Wang, Y.-C. Cheng, C.-J. Tong, M.-T. Lin, *Thin Solid Films* **570**, 262 (2014). https://doi.org/10.1016/j.tsf.2014.03.016

50. A.S. Nowick, B.S. Berry, J.L. Katz, *Anelastic Relaxation in Crystalline Solids* (Academic Press, New York, 1975). https://doi.org/10.1115/1.3423694

51. M.S. Blanter, I.S. Golovin, H. Neuhäuser, H.R. Sinning, *Internal Friction in Metallic Materials: A Handbook* (Springer, Berlin, 2007). https://doi.org/10.1007/978-3-540-68758-0

52. J.Q. Fu, T.L. Song, X.X. Liang, G.J. Zhao, *J. Phys. Conf. Ser.* **574**, 012046 (2015). https://doi.org/10.1088/1742-6596/574/1/012046

53. A. Pansari, V. Gedam, B.K. Sahoo, *Physica B Condens. Matter* **456**, 66 (2015). https://doi.org/10.1016/j.physb.2014.08.008

54. J.L. Snoek, *Physica* **8**, 711 (1941). https://doi.org/10.1016/S0031-8914(41)90517-7

55. D.H. Niblett, J. Wilks, *Adv. Phys.* **9**(33), 1 (1960). https://doi.org/10.1080/00018736000101159

56. A. Granato, K. Lücke, *J. Appl. Phys.* **27**, 583 (1956). https://doi.org/10.1063/1.1722436

57. J.D. Eshelby, *Proc. R. Soc. Lond. Ser. A Math. Phys. Sci.* **197**, 396 (1949). https://doi.org/10.1098/rspa.1949.0072

58. A.K. Maier, D. Mari, I. Tkalcec, R. Schaller, *Acta Mater.* **74**, 132 (2014). https://doi.org/10.1016/j.actamat.2014.04.016

59. T.S. Kê, R.F. Mehl, T.S. Ke, *Metall. Mater. Trans. A Phys. Metall. Mater. Sci.* **30**, 2267 (1999). https://doi.org/10.1007/s11661-999-0238-y

60. W. Benoit, *Mater. Sci. Eng. A* **370**, 12 (2004). https://doi.org/10.1016/j.msea.2003.08.068

61. I.A. Aleksandrov, T.V. Malin, K.S. Zhuravlev, S.V. Trubina, S.B. Erenburg, B. Pecz, Y.V. Lebiadok, *Appl. Surf. Sci.* **515**, 146001 (2020). https://doi.org/10.1016/j.apsusc.2020.146001

62. H. Okumura, Y. Watanabe, T. Shibata, K. Yoshizawa, A. Uedono, H. Tokunaga, S. Koseki, T. Arimura, S. Suihkonen, T. Palacios, *Jpn. J. Appl. Phys.* **61**, 026501 (2022). https://doi.org/10.35848/1347-4065/ac47aa

63. A. Forslund, A.V. Ruban, *Phys. Rev. Mater.* **6**, 013803 (2022). https://doi.org/10.1103/PhysRevMaterials.6.013803

64. G. Schoeck, *Phys. Status Solidi* **32**, 651 (1969). https://doi.org/10.1002/pssb.19690320216

65. P. Gadaud, A. Rivière, *J. Phys. IV* **06**, C8-870 (1996). https://doi.org/10.1051/jp4:19968187

66. J.P. Ngantcha, M. Gerland, Y. Kihn, A. Rivière, *Eur. Phys. J. Appl. Phys.* **29**, 83 (2005). https://doi.org/10.1051/epjap:2004200

67. A. Rivière, V. Pelosin, *J. Alloys Compd.* **310**, 173 (2000). https://doi.org/10.1016/S0925-8388(00)00941-5

68. C. Amrane, D. Hamana, I.S. Golovin, *Mater. Charact.* **134**, 49 (2017). https://doi.org/10.1016/j.matchar.2017.10.013

69. J. Zhai, X. Song, A. Xu, Y. Chen, Q. Han, *Met. Mater. Int.* **27**, 1458 (2021). https://doi.org/10.1007/s12540-019-00566-y □